OPTICA

Nanopatterned parametric oscillators for laser conversion beyond an octave

Grant M. Brodnik,[1,2,*] **Haixin Liu,**[1,2] **David R. Carlson,**[3] **Jennifer A. Black,**[1,4] **and Scott B. Papp**[1,2]

[1] *Time and Frequency Division, National Institute of Standards and Technology, Boulder, Colorado 80305, USA*
[2] *Department of Physics, University of Colorado, Boulder, Colorado 80309, USA*
[3] *Octave Photonics, Louisville, Colorado 80027, USA*
[4] *Current address: Vescent Photonics, Golden, Colorado 80401, USA*
**grant.brodnik@colorado.edu*

Received 29 October 2024; revised 28 January 2025; accepted 6 February 2025; published 27 February 2025

Many uses of lasers place the highest importance on access to specific wavelength bands. For example, mobilizing optical-atomic clocks for a leap in sensing requires compact lasers at frequencies spread across the visible and near-infrared. Integrated photonics enables high-performance, scalable laser platforms. However, customizing laser-gain media to support wholly new bands is challenging and often prohibitively mismatched in scalability to early quantum-based sensing and information systems. Here, we demonstrate a tantalum pentoxide microresonator optical-parametric oscillator (OPO) that converts a pump laser to an output wave within a frequency span exceeding an octave. We control phase matching for oscillation by nanopatterning the microresonator to open a photonic-crystal bandgap on the mode of the pump laser. The photonic crystal splits only the pump mode and preserves the broader mode structure of the resonator, thus affording a single parameter to control output waves across the octave span using a nearly fixed frequency pump laser. We also demonstrate tuning the oscillator in free-spectral-range steps, more finely with temperature, and minimal additive frequency noise of the laser-conversion process. Our work shows that nanophotonic structures offer control of laser conversion in microresonators, bridging phase-matching of nonlinear optics and application requirements for laser designs.

https://doi.org/10.1364/OPTICA.545158

---

1. INTRODUCTION

Sophisticated physical systems with such disparate aims as characterization of biological samples [1], operation of quantum information protocols [2], standards and sensors for time based on optical clocks [3], and precision metrology with optical sources [4] demand versatility in lasers. Especially in the visible to near-infrared, laser-wavelength access in a compact footprint is challenging due to the limited availability and narrow operating ranges of active, or electrically-pumped, laser-gain materials suited to wafer-scale integration. The challenge is solved today by large, tabletop lasers based on solid-state materials and bulk nonlinear optics that provide exceptional flexibility in wavelength range, output power, and temporal profile but with substantial expense and complicated operation that hinders usability in applications.

Semiconductor lasers are less expensive and better engineered to support applications. However, the recurring effort to customize semiconductor gain materials is a barrier in expanding their use. Moreover, achieving high performance in semiconductor lasers requires low-loss components that are often incompatible with high gain. A theme in recent laser development has been the combination of gain and photonics materials. Heterogeneous integration of gain and photonics materials on a common substrate or hybrid integration of independent laser chips and photonics chips can both overcome the challenge of semiconductor material loss, but such laser platforms currently support only select wavelength bands. To date, heterogeneous integration approaches have demonstrated fabrication of lasers on photonic platforms in telecommunications bands [5,6] and more recently below 1 μm [7,8]. Still, a universal laser platform to simultaneously support visible and near-infrared wavelengths remains elusive. Hybrid integration of semiconductor lasers with photonic waveguides has demonstrated co-integration of visible sources with photonics [9], but this approach requires custom packaging and active alignment of gain material with waveguides.

To open up laser-wavelength access in challenging spectral bands, we propose an approach using chip-based nonlinear laser conversion suited to wafer-scale processing with semiconductor gain. Thereby, we leverage advancing laser integration in select wavelength bands, and we develop nonlinear wavelength converters with integrated photonics that is directly compatible with laser integration. This alleviates recursive laser-gain development and provides integration. Nonlinear phase matching in integrated photonics has been extensively studied, however now we include the constraint of compatibility with laser integration. For example, both $\chi^{(2)}$ and $\chi^{(3)}$ nonlinear optical processes have enabled laser

2334-2536/25/030337-06 Journal © 2025 Optica Publishing Group

conversion with integrated photonics, including via harmonic generation [10–15], difference frequency generation [16], four-wave mixing [17–20], and optical-parametric oscillation (OPO) [21–24]. Of these processes, $\chi^{(3)}$ microresonator-based degenerately pumped OPO is particularly appealing because of operation with a single input laser, generation of OPO output waves across wide spectral ranges, and implementation with commonly used integrated photonics.

We design microresonator OPOs by group-velocity dispersion (GVD) engineering with geometry, tailoring microresonator waveguide thickness, radius, and width [21,25]. Microresonator OPOs based on GVD engineering provide phase matching that conserves energy of the pump, signal, and idler waves. Moreover, such OPOs depend upon high quality factor of the microresonator modes for these waves [26,27]. To date, the widest signal-to-idler frequency span in microresonator OPOs have a design target of near-zero GVD between the three waves. Indeed, the current limit in OPO frequency span is the required GVD engineering and challenges in fabricating microresonators with tightly controlled geometry [21–23,25,28]. Moreover, in operating OPOs with visible wavelength output, the increasingly normal material GVD limits control of phase matching through geometry alone.

Recently, OPO designs have augmented GVD engineering by geometry with the inclusion of a nanostructured periodic modulation inscribed on the inner wall of a microresonator. These so called photonic-crystal ring resonators (PhCR) induce coherent backscattering at an optical frequency determined by the nanostructure periodicity [29,30]. This opens an optical bandgap, which has been used to control OPO phase matching with bandgaps at the pump [31,32], at the signal wave [33], and in the bandgap-detuned regime [34]. Importantly, nanostructures and geometry are two independent and direct controls of OPO phase matching. However, the OPO signal-to-idler wave frequency span of such nanophotonic OPO has not been explored, nor has operation employing photonic crystal phase matching in the important near-zero GVD regime.

Here, we report nanopatterned microresonator parametric oscillators, or nanopatterned oscillators, that convert a pump laser to an output wave whose frequency is controllable within a span exceeding an octave. Our devices use fundamental transverse electric (TE0) modes for pump, signal, and idler waves. We use geometric GVD engineering to access the near-zero GVD regime between the OPO waves, and we use a photonic-crystal bandgap to provide phase matching for broadband OPO. This enables robust laser conversion and access to an unprecedented OPO wave frequency span in nanostructured microresonators. Importantly, our approach simplifies the required pump laser tuning range for a microresonator OPO; in our devices this is set by the maximum bandgap, on the order of several 10 s of GHz, resulting in the required pump tuning being four orders of magnitude times less than the achievable OPO wave frequency span. We realize nanopatterned oscillators on the tantalum pentoxide (Ta_2O_5), or tantala, platform, which has high Kerr nonlinearity, low stress, and high quality factor across the visible and near-infrared wavelengths [35]. Moreover, tantala supports GVD engineering [36] and heterogeneous integration [37–39]. Experimentally, we demonstrate nanopatterned oscillators which take a pump laser near 1062 nm and create output OPO signal and idler waves. We demonstrate a maximum OPO wave frequency span from 749 nm to 1806 nm that corresponds to >230 THz with pump-laser tuning <30 GHz. These experiments demonstrate the principle of laser-wavelength access while requiring minimal pump laser tuning, which is a critical innovation for laser-wavelength access on a chip. In view of interest to use the devices for applications, we characterize several aspects of the output OPO, including thermal fine-frequency tuning and additive frequency noise of the laser-conversion process.

2. NANOPHOTONIC WAVELENGTH CONVERTERS

Nanopatterned oscillators enable laser conversion through resonant phase matching of the pump, signal, and idler waves [40]. We characterize the frequency error $\delta f(\mu)$ for phase matching as

$$\delta f(\mu) = 2(f_0 \pm \gamma/2) - f(+\mu) - f(-\mu), \tag{1}$$

where the resonant frequencies of a microresonator are $f(\mu)$ and $\mu = m - m_p$ is the azimuthal mode number, m, relative to the pump, m_p. The pump mode $f(\mu = 0)$ is f_0, which we split with a photonic-crystal bandgap of magnitude γ, thereby shifting its frequency without affecting the GVD design. The pump mode, $f_0 \pm \gamma/2$, phase matches to modes symmetric about the pump, $f(\pm\mu)$, when Eq. (1) is positive to within the pump mode Kerr shift [26,31,33].

We operate nanopatterned oscillators in the near-zero GVD regime and use γ to control the signal and idler wave frequencies with minimal pump laser frequency tuning. Figure 1(a) presents the concept of nanopatterned oscillators where we convert a pump laser with frequency ν_p to signal and idler waves with frequency ν_s and ν_i. We instill γ by inscribing a nanopattern into the microresonator sidewall with modulation amplitude A_{PhC} as seen in Fig. 1(b). Graphically, we can understand nanophotonic oscillator laser conversion through the mode structure depicted in Fig. 1(c). Operationally, we tune the pump laser to resonance $\nu_p = f_0 + \gamma/2$ to initiate OPO-based laser conversion to ν_s and ν_s, which abides strict energy conservation $2\nu_p = \nu_s + \nu_i$ [41].

We realize this method in practice, demonstrating γ-controlled laser conversion. To implement nanopatterned oscillators, we use PhCRs, which provide a broadband and high-finesse microresonator with programmable γ to control OPO phase matching. Figure 1(d) plots δf of this type of nanophotonic oscillator where we see that varying γ enables alignment of $f_0 + \gamma/2$ to different pairs of $f(\pm\mu)$, thereby modifying OPO phase matching to control ν_s and ν_i. We transfer the δf design of Fig. 1(d) to devices in the tantala platform (see Supplement 1), demonstrating laser conversion as seen in Fig. 1(e), in which we plot optical spectra for several γ settings with otherwise identical GVD. The pump ν_p needs to be tuned only several GHz to track $\gamma/2$ while ν_s and ν_i are tuned across ≈ 20 THz with an OPO wave frequency span exceeding 100 THz.

3. DEVICE CHARACTERISTICS

In addition to satisfying Eq. (1) for OPO phase matching, we require a high quality factor to realize nanopatterned oscillators [25,26,42]. To characterize the quality factor of devices, we measure transmission spectra of three widely tunable external cavity lasers near the 980 nm, 1064 nm, and 1300 nm wavelength bands. Figure 2(a) presents the loaded, intrinsic, and coupling quality factors (Q_L, Q_i, and Q_c) as a function of frequency for a single representative device. We measure $Q_i \approx 0.9 \times 10^6$ across the

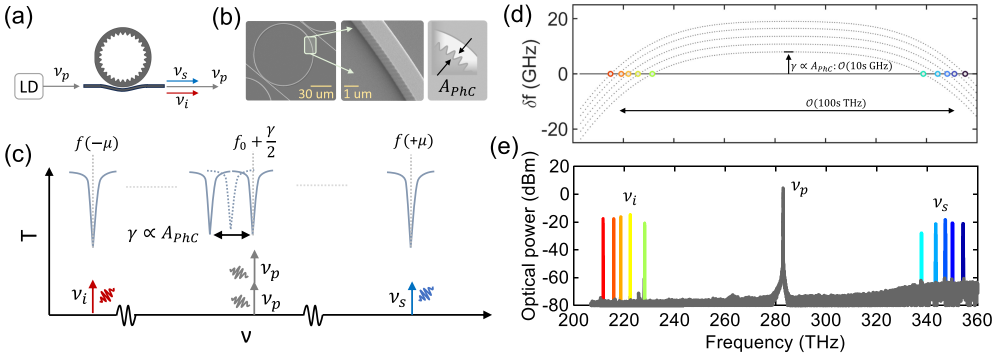

Fig. 1. (a) A laser diode (LD) pumps a nanophotonic oscillator with frequency ν_p for OPO laser conversion to output waves with frequency ν_s and ν_i. (b) Scanning electron microscope (SEM) images of a nanophotonic oscillator highlighting the nanophotonic modulation with amplitude A_PhC. (c) Graphical representation of phase matching that governs resonant OPO processes in a nanophotonic oscillator. (d) Frequency error, δf, of Eq. (1). As we increase γ, different resonant modes $f(\pm\mu)$ are brought into phase matching for OPO. (e) Corresponding off-chip optical spectra of nanophotonic oscillation for devices with the same nominal δf shown in (d), and varying γ.

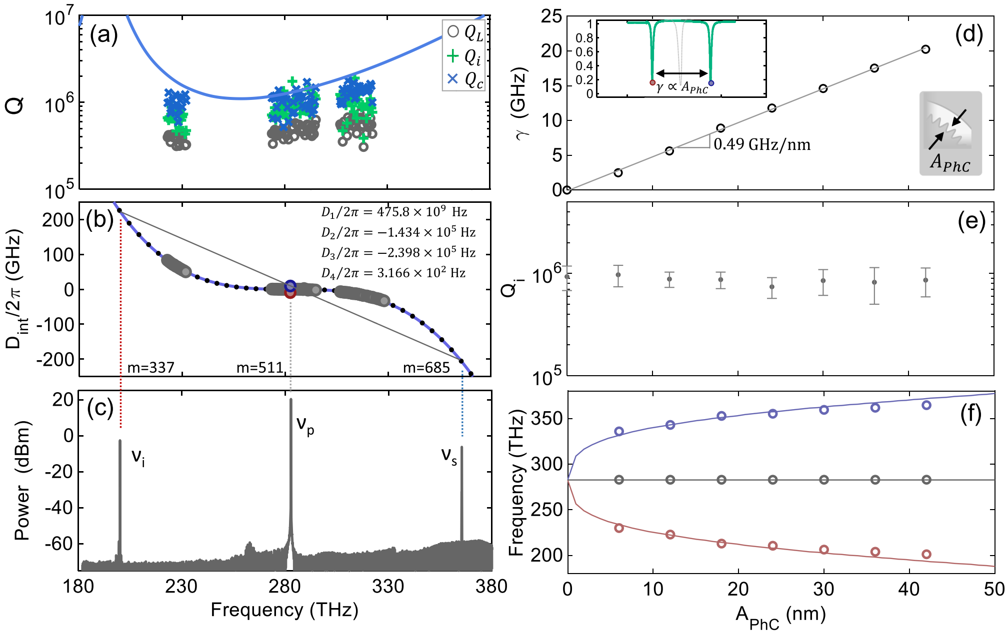

Fig. 2. (a) Measured Q_L, Q_i, and Q_c (colored markers) across three spectral regions and modeled Q_c (blue line). (b) Experimental (gray circles), modeled (black dots), and polynomial fit of modeled (blue line) $D_\mathrm{int}/2\pi$. Dispersion parameters are given for the polynomial fit [see Eq. (2)]. Blue and red circles denote the upshifted and downshifted photonic crystal modes, respectively. (c) OPO spectrum for the device characterized in (a) and (b), calibrated to show on-chip power after accounting for chip insertion loss. (d) Measured γ versus A_PhC. The left inset shows example pump resonance $f_0 \pm \gamma/2$, and the right inset shows A_PhC inner sidewall modulation. (e) Q_i vs. A_PhC. (f) Measured (circles) and modeled (lines) OPO frequencies vs. A_PhC, highlighting nanophotonic control of OPO.

three wavelength bands, suitable for efficient OPO. Moreover, we measure the wavelength-dependent Q_c to agree with three-dimensional, finite-difference time-domain modeling within fabrication tolerance (see Supplement 1) [43]. For all measurements, we couple light into and out of the chip using HI1060 lensed fiber with a manufactured spot size of 2 μm and measure chip-to-fiber insertion loss to be 6 ± 0.5 dB per facet.

To explore the accuracy of γ-controlled phase matching in our nanopatterned oscillators, we measure the GVD and pump the devices above the OPO threshold power to validate Eq. (1). We express the resonant angular frequencies, ω, of a microresonator as a function of μ using a Taylor expansion:

$$\begin{aligned}\omega(\mu) &= 2\pi f(\mu) = 2\pi f_0 + D_1\mu + \frac{D_2\mu^2}{2} + \frac{D_3\mu^3}{6} + \ldots \\ &= \omega_0 + D_1\mu + D_\mathrm{int}.\end{aligned} \quad (2)$$

The integrated dispersion, D_int, relates the change in resonant angular frequencies relative to the free spectral range ($\mathrm{FSR} = D_1/2\pi$) at the pump [44]. From our measured transmission spectra, we can directly determine D_int and compare with finite element method simulations of the microresonator eigenfrequencies (see Supplement 1 for more). For the same device characterized in Fig. 2(a), Fig. 2(b) presents a measured (gray circles), modeled (black dots), and polynomial fit of modeled (blue line) $D_\mathrm{int}/2\pi$. Dispersion parameters are given for the polynomial fit of Eq. (2). Blue and red circles denote the upshifted- and downshifted-frequency photonic crystal modes, respectively. We find the nanophotonic oscillator pump resonance $f_0 + \gamma/2$ with $m_\mathrm{p} = 511$ satisfies Eq. (1) at modes $m = 685$ and $m = 337$ ($\mu = \pm 174$). In terms of D_int, OPO phase matching occurs when we can draw a straight line through $f_0 + \gamma/2$ and $f(\pm\mu)$ as seen in Fig. 2(b) [41]. For this device, the geometric GVD is designed such that phase matching occurs using the blue-shifted photonic crystal mode. We validate phase matching by pumping the nanophotonic oscillator with D_{int} from Fig. 2(b) and recording the OPO spectrum, calibrated to represent on-chip powers, as seen in Fig. 2(c). We find that when pumping $f_0 + \gamma/2$ at $\nu_{\text{p}} = 282.8$ THz, the nanophotonic oscillator provides laser conversion to output waves with frequencies $\nu_{\text{s}} = 365.5$ THz and $\nu_{\text{i}} = 200.1$ THz. We measure threshold, P_{th}, of this device to be 84 ± 4 mW and operate the device at $\sim 1.3 P_{\text{th}}$ in Fig. 2(c). We note that while using a photonic crystal on the pump mode offers robust control over phase matching, such operation results in a four-times increase in OPO threshold compared to conventional OPO devices due to the coupling of forward- and backward-propagating pump fields [27]. As pump power increases, we observe mode hopping due to power-dependent Kerr and thermal shifts in phase matching [33]. Continuously single-mode operation and decreased sensitivity to such shifts can be realized using designs with a photonic crystal on the OPO signal mode [33], while threshold and conversion efficiency can be improved using waveguide reflectors to recirculate the pump field [27] and with careful design of bus-ring coupling that considers pump, signal, and idler modes independently [42,43].

Deterministic control of γ is of critical importance for laser conversion with nanopatterned oscillators. Therefore, we characterize γ as a function of A_{PhC} and find a linear response with slope ≈ 0.5 GHz/nm up to $A_{\text{PhC}} = 50$ nm as seen in Fig. 2(d). Remarkably, despite the presence of the nanostructure, we measure little Q_{i} variation or degradation over the full range of $\gamma < 25$ GHz as seen in Fig. 2(e). We control the laser conversion process by use of A_{PhC} as shown in Fig. 2(f). Here, we find that $A_{\text{PhC}} < 50$ nm results in a large change of OPO phase matching governed by Eq. (1), with control of both ν_{s} and ν_{i} across > 50 THz and maximum OPO wave frequency span exceeding 150 THz of optical bandwidth.

4. FREQUENCY DESIGN AND CONTROL

Leveraging nanopatterned oscillators, we demonstrate wavelength access beyond an octave through γ-controlled laser conversion. We measure OPO spectra of devices pumped above threshold, and we extract ν_{s} and ν_{i} to determine the output OPO signal-to-idler frequency span, which we denote as $\Delta\nu_{\text{OPO}} = \nu_{\text{s}} - \nu_{\text{i}}$. For a family of devices with negative D_2 that realize phase matching using the red-shifted photonic crystal mode, we show in Fig. 3(a) measurements (points) and modeling (line) of $\Delta\nu_{\text{OPO}}$ as a function of γ, predicted by the phase-matching condition of Eq. (1). Figure 3(b) presents a compilation of measured output OPO wave frequencies, ν_{s}, ν_{i}, which we denote as the ν_{output} (points) for various nanopatterned oscillators and compare with the Eq. (1) prediction, which we denote as ν_{design} (line) of the OPO; see Supplement 1. These data assess the maximum wave span of the OPO.

Provided the wavelength access of nanopatterned oscillators, we characterize other important operational details for applications, including thermal frequency tuning and power-spectral noise density of output waves. Figure 3(c) shows the variation of OPO wave frequencies in a single device as we vary the temperature from 10°C to 70° by use of a thermoelectric cooler. At room temperature, $\text{T} = 20°\text{C}$, $\nu_{\text{s}} = 365.5$ THz, and $\nu_{\text{i}} = 200.1$ THz ($\Delta\nu_{\text{OPO}} = 165.4$ THz). We then measure the three OPO waves as a function of temperature $\nu_{\text{s,p,i}}(T)$ and

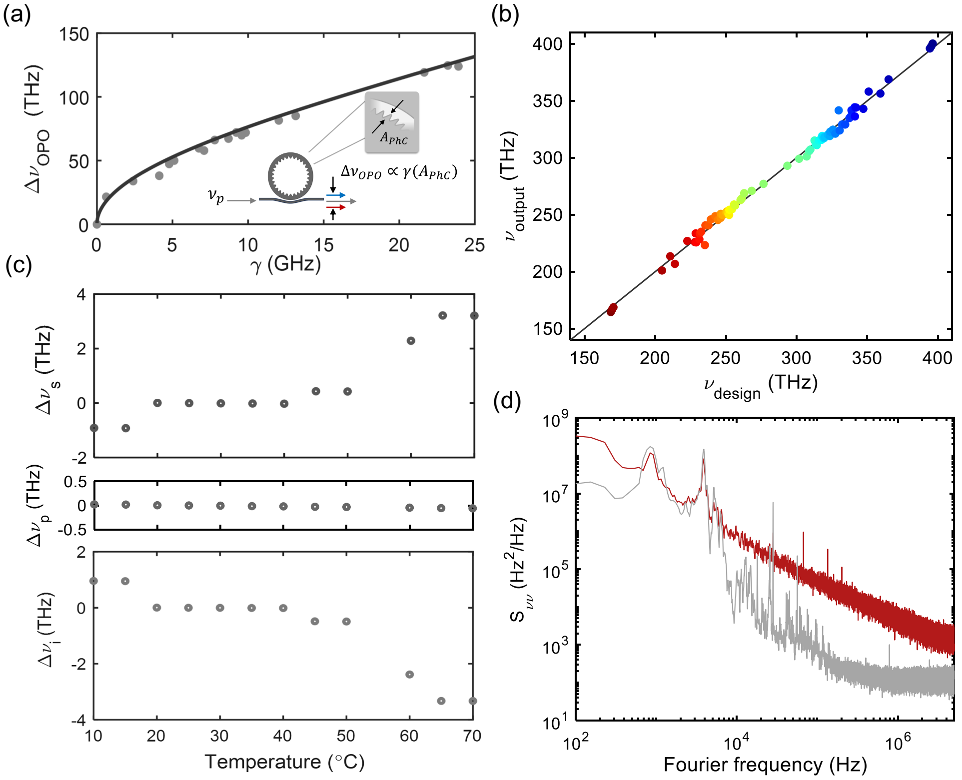

Fig. 3. (a) Measured (points) and modeled (line) $\Delta\nu_{\text{OPO}}$ as a function of γ for an otherwise fixed GVD. (b) Measured (points) and modeled (line) ν_{output} versus ν_{design}. (c) Thermal response of OPO wave frequencies in a single nanophotonic oscillator. (d) Measured frequency noise for an OPO with $\nu_{\text{p}} = 282.8$ THz (gray) and $\nu_{\text{i}} = 219.3$ THz (red).

plot the variation from the room temperature measurement, $\Delta\nu_{\mathrm{s,p,i}} = |\nu_{\mathrm{s,p,i}}(20^\circ\mathrm{C}) - \nu_{s,p,i}(T)|$. During thermal tuning, we shift ν_{p} to track the thermo-optic shift of the pump resonance mode with slope ≈ -1.4 GHz/C, consistent with tantala's reported thermo-optic coefficient [35]. However, across the measured temperature range, ν_{s} and ν_{i} tune by ≈ 4 THz discontinuously, which we attribute to thermally sensitive phase matching [21]. We also measure the optical frequency noise power spectral density, $S_\nu(f)$, for ν_{p} and ν_{i} [Fig. 3(d)], calculating the integral linewidth by use of the $1/\pi$ and β-separation techniques [45,46]. We find the pump laser ($\nu_{\mathrm{p}} = 282.8$ THz) to have a $1/\pi$-integrated linewidth of 28 ± 3 kHz and a β-separation linewidth of 862 ± 61 kHz integrated down to Fourier frequency of 78 Hz. The corresponding free-running $\nu_{\mathrm{i}} = 219.3$ THz has a $1/\pi$-integrated linewidth of 89 ± 6 kHz and a β-separation linewidth of 1.03 ± 0.07 MHz. We attribute the additional optical-frequency noise of ν_{i} to thermo-refractive noise [47,48] due to the characteristic bandwidth of the power-spectral density.

5. DISCUSSION

In summary, we have demonstrated a nanophotonic approach to achieve phase matching for broadband OPO laser conversion into the visible and near-infrared. Moreover, thermal fine-frequency tuning and the laser conversion process contribute minimal additive frequency noise in nanopatterned oscillators. By leveraging the precise phase-matching control afforded by nanopatterning, we realize laser conversion spanning more than an octave with required pump laser tunability of only tens of gigahertz. Nanopatterned oscillators enable the broadband, configurable gain afforded by nonlinear optics to operate in concert with existing integrated pump lasers, avoiding the necessity to re-customize laser gain materials in underdeveloped spectral regions. Thereby, nanopatterned oscillators address the challenge of laser-wavelength access, in particular, reaching across the short-wave infrared and into the visible.

Funding. Defense Advanced Research Projects Agency (HR0011-20-2-0046); Air Force Office of Scientific Research (FA9550-20-1-0004 Project Number 19RT1019); National Science Foundation (OMA - 2016244); National Institute of Standards and Technology.

Acknowledgment. We thank Lindell Williams and Yan Jin for reviewing the paper.

Disclosures. The authors declare no competing interests. This work is a contribution of the US Government and is not subject to US copyright. Mention of specific companies or trade names is for scientific communication only and does not constitute an endorsement by NIST.

Data availability. The data that support the plots within this paper and other findings of this study are available from the corresponding author upon reasonable request.

Supplemental document. See Supplement 1 for supporting content.

REFERENCES

1. D. Ozcelik, A. Jain, A. Stambaugh, *et al.*, "Scalable spatial-spectral multiplexing of single-virus detection using multimode interference waveguides," Sci. Rep. **7**, 12199 (2017).
2. J. M. Pino, J. M. Dreiling, C. Figgatt, *et al.*, "Demonstration of the trapped-ion quantum CCD computer architecture," Nature **592**, 209–213 (2021).
3. W. F. McGrew, X. Zhang, H. Leopardi, *et al.*, "Towards the optical second: verifying optical clocks at the SI limit," Optica **6**, 448–454 (2019).
4. T. Bothwell, C. J. Kennedy, A. Aeppli, *et al.*, "Resolving the gravitational redshift across a millimetre-scale atomic sample," Nature **602**, 420–424 (2022).
5. D. Huang, M. A. Tran, J. Guo, *et al.*, "High-power sub-kHz linewidth lasers fully integrated on silicon," Optica **6**, 745–752 (2019).
6. J. Guo, C. Xiang, T. J. Morin, *et al.*, "E-band widely tunable, narrow linewidth heterogeneous laser on silicon," APL Photon. **8**, 046114 (2023).
7. M. A. Tran, C. Zhang, T. J. Morin, *et al.*, "Extending the spectrum of fully integrated photonics to submicrometre wavelengths," Nature **610**, 54–60 (2022).
8. Z. Zhang, B. Shen, M. A. Tran, *et al.*, "Photonic integration platform for rubidium sensors and beyond," Optica **10**, 752–753 (2023).
9. M. Corato-Zanarella, A. Gil-Molina, X. Ji, *et al.*, "Widely tunable and narrow-linewidth chip-scale lasers from near-ultraviolet to near-infrared wavelengths," Nat. Photonics **17**, 157–164 (2023).
10. T. Carmon and K. J. Vahala, "Visible continuous emission from a silica microphotonic device by third-harmonic generation," Nat. Phys. **3**, 430–435 (2007).
11. A. W. Bruch, X. Liu, J. B. Surya, *et al.*, "On-chip χ^2 microring optical parametric oscillator," Optica **6**, 1361–1366 (2019).
12. L. Chang, Y. Li, N. Volet, *et al.*, "Thin film wavelength converters for photonic integrated circuits," Optica **3**, 531–535 (2016).
13. E. Nitiss, J. Hu, A. Stroganov, *et al.*, "Optically reconfigurable quasi-phase-matching in silicon nitride microresonators," Nat. Photonics **16**, 134–141 (2022).
14. D. D. Hickstein, D. R. Carlson, H. Mundoor, *et al.*, "Self-organized nonlinear gratings for ultrafast nanophotonics," Nat. Photonics **13**, 494–499 (2019).
15. T. P. McKenna, H. S. Stokowski, V. Ansari, *et al.*, "Ultra-low-power second-order nonlinear optics on a chip," Nat. Commun. **13**, 4532 (2022).
16. E. Sahin, B. Zabelich, O. Yakar, *et al.*, "Difference-frequency generation in optically poled silicon nitride waveguides," Nanophotonics **10**, 1923–1930 (2021).
17. M. A. Foster, A. C. Turner, J. E. Sharping, *et al.*, "Broad-band optical parametric gain on a silicon photonic chip," Nature **441**, 960–963 (2006).
18. X. Lu, G. Moille, Q. Li, *et al.*, "Efficient telecom-to-visible spectral translation through ultralow power nonlinear nanophotonics," Nat. Photonics **13**, 593–601 (2019).
19. Z. Ye, P. Zhao, K. Twayana, *et al.*, "Overcoming the quantum limit of optical amplification in monolithic waveguides," Sci. Adv. **7**, eabi8150 (2021).
20. J. Riemensberger, N. Kuznetsov, J. Liu, *et al.*, "A photonic integrated continuous-travelling-wave parametric amplifier," Nature **612**, 56–61 (2022).
21. X. Lu, G. Moille, A. Rao, *et al.*, "On-chip optical parametric oscillation into the visible: generating red, orange, yellow, and green from a near-infrared pump," Optica **7**, 1417–1425 (2020).
22. Y. Sun, J. Stone, X. Lu, *et al.*, "Advancing on-chip Kerr optical parametric oscillation towards coherent applications covering the green gap," Light Sci. Appl. **13**, 201 (2024).
23. N. L. B. Sayson, T. Bi, V. Ng, *et al.*, "Octave-spanning tunable parametric oscillation in crystalline Kerr microresonators," Nat. Photonics **13**, 701–706 (2019).
24. L. Ledezma, A. Roy, L. Costa, *et al.*, "Octave-spanning tunable infrared parametric oscillators in nanophotonics," Sci. Adv. **9**, eadf9711 (2023).
25. X. Lu, G. Moille, A. Singh, *et al.*, "Milliwatt-threshold visible–telecom optical parametric oscillation using silicon nanophotonics," Optica **6**, 1535–1541 (2019).
26. J. R. Stone, G. Moille, X. Lu, *et al.*, "Conversion efficiency in Kerr-microresonator optical parametric oscillators: from three modes to many modes," Phys. Rev. Appl. **17**, 024038 (2022).
27. H. Liu, G. M. Brodnik, J. Zang, *et al.*, "Threshold and laser conversion in nanostructured-resonator parametric oscillators," Phys. Rev. Lett. **132**, 023801 (2024).
28. R. R. Domeneguetti, Y. Zhao, X. Ji, *et al.*, "Parametric sideband generation in CMOS-compatible oscillators from visible to telecom wavelengths," Optica **8**, 316–322 (2021).
29. X. Lu, S. Rogers, W. C. Jiang, *et al.*, "Selective engineering of cavity resonance for frequency matching in optical parametric processes," Appl. Phys. Lett. **105**, 151104 (2014).

30. S.-P. Yu, D. C. Cole, H. Jung, *et al.*, "Spontaneous pulse formation in edgeless photonic crystal resonators," Nat. Photonics **15**, 461–467 (2021).
31. J. A. Black, G. M. Brodnik, H. Liu, *et al.*, "Optical-parametric oscillation in photonic-crystal ring resonators," Optica **9**, 1183–1189 (2022).
32. X. Lu, A. Chanana, F. Zhou, *et al.*, "Kerr optical parametric oscillation in a photonic crystal microring for accessing the infrared," Opt. Lett. **47**, 3331–3334 (2022).
33. J. R. Stone, X. Lu, G. Moille, *et al.*, "Wavelength-accurate nonlinear conversion through wavenumber selectivity in photonic crystal resonators," Nat. Photonics **18**, 192–199 (2024).
34. Y. Jin, E. Lucas, J. Zang, *et al.*, "The bandgap-detuned excitation regime in photonic-crystal resonators," arXiv (2024).
35. H. Jung, S.-P. Yu, D. R. Carlson, *et al.*, "Tantala Kerr nonlinear integrated photonics," Optica **8**, 811–817 (2021).
36. J. A. Black, R. Streater, K. F. Lamee, *et al.*, "Group-velocity-dispersion engineering of tantala integrated photonics," Opt. Lett. **46**, 817–820 (2021).
37. M. Jafari, T. Fatema, D. R. Carlson, *et al.*, "Heterogeneous integration of AlGaAs/GaAs photodiodes on tantala waveguides for visible-light applications," in *Conference on Lasers and Electro-Optics (CLEO)* (IEEE, 2022), pp. 1–2.
38. A. E. Dorche, N. Nader, E. J. Stanton, *et al.*, "Heterogeneously integrated near-infrared DFB laser on tantalum pentoxide," in *Optical Fiber Communication Conference* (Optica, 2023), paper Tu3C-6.
39. D. J. Blumenthal, "Photonic integration for UV to IR applications," APL Photon. **5**, 020903 (2020).
40. T. J. Kippenberg, S. M. Spillane, and K. J. Vahala, "Kerr-nonlinearity optical parametric oscillation in an ultrahigh-Q toroid microcavity," Phys. Rev. Lett. **93**, 083904 (2004).
41. J. A. Black, Z. L. Newman, S.-P. Yu, *et al.*, "Nonlinear networks for arbitrary optical synthesis," Phys. Rev. X **13**, 021027 (2023).
42. J. R. Stone, X. Lu, G. Moille, *et al.*, "Efficient chip-based optical parametric oscillators from 590 to 1150 nm," APL Photon. **7**, 121301 (2022).
43. G. Moille, Q. Li, T. C. Briles, *et al.*, "Broadband resonator-waveguide coupling for efficient extraction of octave-spanning microcombs," Opt. Lett. **44**, 4737–4740 (2019).
44. S. Fujii and T. Tanabe, "Dispersion engineering and measurement of whispering gallery mode microresonator for Kerr frequency comb generation," Nanophotonics **9**, 1087–1104 (2020).
45. W. Liang, V. Ilchenko, D. Eliyahu, *et al.*, "Ultralow noise miniature external cavity semiconductor laser," Nat. Commun. **6**, 7371 (2015).
46. G. Di Domenico, S. Schilt, and P. Thomann, "Simple approach to the relation between laser frequency noise and laser line shape," Appl. Opt. **49**, 4801–4807 (2010).
47. Y. Zhao, J. K. Jang, G. J. Beals, *et al.*, "All-optical frequency division on-chip using a single laser," Nature **627**, 546–552 (2024).
48. T. E. Drake, J. R. Stone, T. C. Briles, *et al.*, "Thermal decoherence and laser cooling of Kerr microresonator solitons," Nat. Photonics **14**, 480–485 (2020).